

# Not All Regions Are Equal: Attention-Guided Perturbation Network for Industrial Anomaly Detection

Tingfeng Huang<sup>\*a</sup>, Weijia Kong<sup>\*a</sup>, Yuxuan Cheng<sup>a</sup>, Jingbo Xia<sup>a</sup>, Rui Yu<sup>b</sup>, Jinhai Xiang<sup>a</sup>,  
Xinwei He<sup>†a</sup>

<sup>a</sup>*Huazhong Agricultural University, {kst0D83, wjkong, hxxss, xjb, jimmy\_xiang, xwhe}@mail.hzau.edu.cn*

<sup>b</sup>*University of Louisville, rui.yu@louisville.edu*

---

## Abstract

In unsupervised image anomaly detection, reconstruction methods aim to train models to capture normal patterns comprehensively for normal data reconstruction. Yet, these models sometimes retain unintended reconstruction capacity for anomalous regions during inference, leading to missed detections. To mitigate this issue, existing works perturb normal samples in a sample-agnostic manner, uniformly adding noise across spatial locations before reconstructing the original. Despite promising results, they disregard the fact that foreground locations are inherently more critical for robust reconstruction. Motivated by this, we present a novel reconstruction framework named Attention-Guided Perturbation Network (AGPNet) for industrial anomaly detection. Its core idea is to add perturbations guided by a sample-aware attention mask to improve the learning of invariant normal patterns at important locations. AGPNet consists of two branches, *i.e.*, a reconstruction branch and an auxiliary attention-based perturbation one. The reconstruction branch learns to reconstruct normal samples, while the auxiliary one aims to produce attention masks to guide the noise perturbation process for normal samples. By perturbing more aggressively at those important regions, we encourage the reconstruction branch to learn inherent normal patterns both comprehensively and robustly. Extensive experiments are conducted on several popular benchmarks covering MVTec-AD, VisA, and MVTec-3D, and show that AGPNet consistently obtains leading anomaly detection performance across a variety of setups, including few-shot, one-class, and multi-class ones.

---

\* Authors contribute equally. † Corresponding author.

*Key words:*

Unsupervised Image Anomaly Detection, Reconstruction, Perturbation, Attention.

---

## 1. Introduction

Automatically detecting and localizing anomalies in industrial images has extensive applications in manufacturing [1, 2]. However, this task typically encounters the challenge of *cold-start* [3] where gathering normal samples is easy, whereas acquiring anomalous samples is costly or infeasible. In recent years, significant effort has been devoted to developing unsupervised anomaly detection (UAD) algorithms [4, 5, 6, 7, 8] that learn to model normality distribution with *solely* normal images. In general, these methodologies can be further divided into three types [9, 10]: *Embedding-based* [11, 2], *Synthesizing-based* [3, 6, 12], and *Reconstruction-based* [13, 14, 15]. While embedding- and synthesis-based methods often rely on intricate designs, reconstruction-based approaches are more straightforward with superior scalability [16] and have thus been extensively studied.

Reconstruction methods currently represent the state-of-the-art. They rely on one core assumption: **reconstruction networks exposed to normal data alone can reconstruct normal ones well, but find difficulty in reconstructing abnormal ones.** Thus, an anomaly map can be computed by analyzing the reconstruction error of the input. As per this assumption, some methods attempt to reconstruct input images with popular generative models, *i.e.*, AutoEncoder [17, 18, 4], GANs [19, 20, 21], or Diffusion-based models [22, 23]. However, reconstructing raw pixel values usually fails when normal and anomalous regions share similar values [24]. Another direction is reconstructing features since they provide more contextual information than raw pixels [24, 25, 26]. With the availability of large pretrained networks, there has been a growing interest in learning to reconstruct discriminative features from models pretrained on large-scale datasets, *e.g.*, ImageNet [27].

**The assumption, however, sometimes fails, as networks may reconstruct anomalies unpredictably.** To address this, prior work employs input perturbation and then maps them to normal ones to suppress anomaly reconstruction (Figure. 1(a)). For instance,  
*Preprint submitted to Neural Networks* *November 19, 2025*

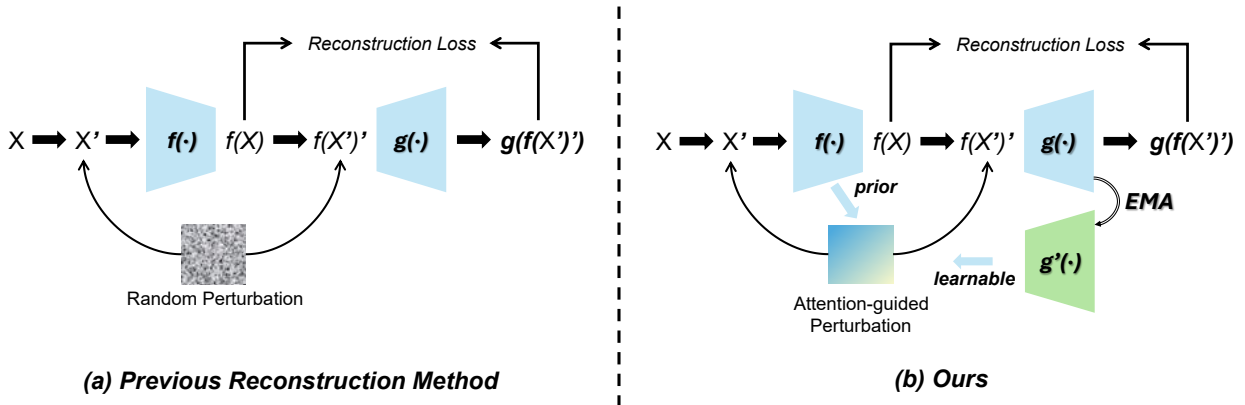


Figure 1: Comparisons between ours and existing perturbation strategies in reconstruction paradigm for anomaly detection. Compared with (a) existing networks adopting fixed or random perturbations, (b) we introduce to learn to guide the perturbation with sample-aware masks from the network and help to learn a better reconstruction model.

AESc [28] introduces a stain perturbation model to corrupt the image. SCADN [21] generates fixed multi-scale striped masks to erase parts of regions in the input and learn to reconstruct the missing information. DRAEM [3] obtains promising results by recovering pseudo-anomaly disturbed normal images. UniAD [26] perturbs the features uniformly with noise. By perturbing the input, the reconstruction network is forced to learn invariant patterns for reconstruction. However, these works simply apply fixed or random masks to perturb input images/features indiscriminately, regardless of their specific contextual and semantic characteristics. In real-world industrial settings where there exists *diverse* categories and varying shapes and sizes of objects, such information provides important prior and could be utilized as auxiliary guidance to strengthen normal feature learning.

Motivated by above, in this paper, we propose to learn a reconstruction model by considering **sample-specific content and structural priors for perturbation**. To this end, we introduce a simple yet effective reconstruction framework named **AGPNet** (Figure. 2) for unsupervised anomaly detection. The core idea behind our framework is to perturb the normal input according to the importance of each location during training. This approach enables the reconstruction network to pay more attention to those important areas, thereby

learning *invariant normal patterns* more compactly and efficiently. To achieve this goal, we carefully design an auxiliary branch that generates attention masks for the noise-adding process (Figure. 1(b)). Specifically, the auxiliary branch combines two important cues to derive the final attention masks. The first is the attention maps from the pre-trained feature extraction layers, which provide strong prior on foreground pixels and important localization cues for the reconstruction network. For instance, industrial categories like screws or tooth-brushes typically have small foreground areas while textures may have complex structures occupying the whole image. Thus, it would be more efficient and beneficial to pay attention to these important locations. The second cue is the attention maps from the momentum distillation [29] of decoder layers from the main branch, which indicate the importance of each location for the reconstruction task. With this cue, the auxiliary branch dynamically emulates the role of the reconstruction network, thereby preventing training stagnation by perturbing important localizations more aggressively as training progresses. Finally, we perturb the normal input at the main branch with simple Gaussian noise weighted by the final attention masks. This process further helps the framework reason about invariant normal patterns at both low and high levels.

Our framework has several desirable merits. **First**, it identifies anomalies at high accuracy under both one-class and multi-class settings. By perturbing more aggressively on the important regions, we are in fact attempting to synthesize hard anomalous locations for training, which helps to learn more discriminative and compact boundaries to spot the abnormal patterns. Besides, the attention masks are sample-aware, accommodating images from diverse categories that exhibit different anomaly types. **Second**, it is more efficient to train. Anomalies in industrial images usually exhibit diverse structures and textures scattered across *any* foreground locations. Some anomalies can be easily identified by reconstructing them based on proximal pixels with similar colors, while anomalies with irregular structures near the contour or local edge pixels pose a challenge for reconstruction. Masking these critical areas is more conducive to representation learning for reconstruction. **Lastly**, it is a concise and effective framework. The main branch is just constructed with a pretrained backbone followed by a simple ViT-based decoder, and the auxiliary branch will

be *removed* after training, incurring no computation cost for inference.

Empirical results show that AGPNet greatly improves industrial anomaly detection accuracy. For instance, with only 500 epochs of training, it achieves 98.0% P-AUC and 98.7% I-AUC on MVTec-AD [1] under multi-class setting, outperforming UniAD [26] with 1000 epochs of training by +1.2% and +2.2%, respectively.

Our contributions can be summarized as follows:

- We present a simple yet effective framework named AGPNet, which integrates a simple reconstruction network with a novel perturbation scheme. Unlike existing perturbation schemes that treat each spatial location equally, it can apply more targeted perturbations to crucial areas for each sample to enhance the reconstruction process.
- We propose to calculate the attention masks based on prior and learnable attention from the reconstruction network. These masks serve to guide the reconstruction network in learning normal patterns across diverse industrial images.
- Extensive experiments show that AGPNet obtains superior performance on both multi-class and one-class settings, compared with existing state-of-the-arts. Besides, it can also be versatily and effectively extended to the few-shot setup.

## 2. Related Work

### 2.1. Unsupervised Visual Anomaly Detection

Due to the uncertain and scarce nature of visual anomalies, a dominant direction in this area is to formulate this problem as an unsupervised paradigm, also known as unsupervised anomaly detection. It assumes that all images in the training set are normal while the test set contains both normal and abnormal images. A great deal of work has been proposed, for more comprehensive surveys, see [30, 31]. Generally, they can be broadly divided into three groups: synthesizing-based, embedding-based, and reconstruction-based methods.

**Synthesizing-based methods** [32, 33, 34, 3] synthesize anomalies for training. For instance, DRAEM [3] attempts to blend predefined texture images with normal samples.

CutPaste [32] simply cuts an image patch and randomly pastes it to another image location. These methods heavily rely on the synthesized anomaly quality. However, due to the uncertainty and unpredictability of anomalies, it is impossible to synthesize all types of real anomalies with high fidelity.

**Embedding-based methods** [2, 35, 36, 37] typically work by first utilizing pretrained models to embed normal images and then employing statistical models to model the normal distributions. During testing, samples are regarded as being abnormal if they are far away from the normal distributions. For instance, PaDiM [2] models embedded patch features with multivariate Gaussian distribution. PatchCore [35] exploits memory banks to store nominal features. However, they generally demand more computational resources to store the normal embeddings for the training set. In addition, the computing process to identify anomalies during inference is also time-consuming.

**Reconstruction-based methods** [38, 39, 40] hold the assumption that the model pretrained only on normal data can reconstruct normal samples while finding difficulty in reconstructing anomalous during inference. However, this assumption sometimes is not satisfied because of the strong and uncontrollable generalization of deep neural networks. Therefore, many strategies have been proposed to address this issue. Some methods try to add prior from the images [40, 25, 41] as guidance for reconstructions. For instance, P-Net [40] proposes to feed the structure features into the reconstruction network. Other methods [28, 42, 43] frame anomaly detection as the image restoration problem by corrupting the selected content in the images and then learning to restore the corruptions. several methods [44, 38] take the idea of image inpainting by first masking the image randomly and then learning to recover it.

Despite promising results, the above methods focus on the “*one for one*” paradigm, which trains one separate model for each category and thus is more computationally expensive. Recently, some researchers have shifted their attention to another challenging “one for all” paradigm, which only has to train a *single* for all categories. UniAD [26] is the pioneering work for this task. It observes that under this setup the reconstruction network more easily falls into “identical shortcut” problem. They further introduce learnable queries to

the transformer network. Later, OmniAL [45] proposes a panel-guided anomaly synthesis method to prevent the model from performing identical reconstruction. RLR [46] introduces learnable reference representations to force the framework to learn normal feature patterns explicitly for all categories. MoeAD [47] is the first to incorporate Mixture of Experts (MoE) technology into reconstruction-based anomaly detection frameworks.

Following previous works, our work is also reconstruction-based but deals with both “one for one” and “one for all” paradigms. Unlike most existing methods of designing sophisticated architectures, we present a perturbation scheme that could effectively force a simple ViT-based reconstruction decoder to learn invariant normal features. Compared with other perturbation schemes treating each spatial location equally, we use attention masks calculated from the model itself to guide the perturbation. By doing so, our reconstruction network can have a better understanding of the intrinsic and important local normal patterns, which help suppress the anomaly reconstructions effectively.

## *2.2. Few-shot Visual Anomaly Detection*

Recent research has begun to focus on a more challenging task setting: few-shot anomaly detection. It deals with scenarios where only a few training samples are available. RegAD [48] employs a siamese network architecture to train a registration network, calculating the Mahalanobis distance between the features of the test image and those of a support set containing only normal samples for anomaly detection. With the rise of vision-language models, WinCLIP+ [49] introduces CLIP [50] for few-shot anomaly detection. PromptAD [51] further develops on CLIP, leveraging manually designed and learned anomaly prompts to expand the distance between anomalous and normal features, thereby assisting in anomaly detection.

Our framework can also be effectively extended to few-shot anomaly detection. Compared with existing works, our works does not rely additional expensive memory bank. With the simple yet effective attention-based perturbation scheme, our framework is also sample-efficient, obtaining comparable performance to the current leading few-shot anomaly detection methods.

### 3. Method

#### 3.1. Problem Formulation

Following previous works [3, 26], we adopt the reconstruction paradigm for visual anomaly detection. Given a training set  $\mathcal{X}_{train} = \{I_{normal}^i\}_{i=1}^N$  comprising *only normal* samples, our main goal is to train a reconstruction model  $f(\cdot)$  to accurately identify both pixel and image-level anomalies in a test set  $\mathcal{X}_{test} = \{I^j\}_{j=1}^M$  containing both normal and abnormal samples. Note that the problem of VAD can be further divided into two settings: *one-class* and *multi-class*. The one-class setting involves training individual models with images from each semantic category, while the multi-class setting aims to train a unified model with all images from diverse semantic categories. The latter is more computationally efficient due to the  $\mathcal{O}(1)$  task complexity regardless of the semantic category number. Yet it is more challenging due to the diverse distributions of different categories, making it difficult to learn compact representations. Lastly, in addition to conventional unsupervised anomaly detection, our framework can also be versatilly extended to few-shot anomaly detection. In this setup, only a few normal images are provided for training.

#### 3.2. AGPNet

##### 3.2.1. Model Overview

As shown in Figure. 2, our framework mainly consists of two branches. The main reconstruction branch aims to reconstruct the inputs, while the auxiliary branch aims to generate attention masks to guide the perturbation process for the inputs. With the attention mask as perturbation guidance, the reconstruction network tends to learn invariant normal patterns at those crucial locations. After training, the framework can be used for anomaly detection directly by comparing the input and output of the decoder directly, with the discrepancy indicating the anomaly locations. Below we describe each component in detail.

##### 3.2.2. The detail of AGPNet

In the main reconstruction branch, we first utilize a frozen backbone to extract image representations and then utilize a lightweight decoder to learn to perform feature recon-



normalization individually, followed by summation:

$$F_{\text{clean}} = \sum_{l=1}^L \sigma(F_l), \quad (1)$$

which will serve as the reconstruction target and be perturbed for further processing by the decoder.

Another important reason to utilize DINO [53] is that it is a vision-transformer-based architecture and its attention weights can be leveraged to generate the attention mask to guide the decoder training with *minimal efforts*. Therefore, in addition to the  $L$  outputs, we propose to reuse the associated attention maps, denoted by  $A_l \in \mathbb{R}^{H_l \times W_l}$ , to provide the important prior cues for the image to guide the training of the decoder. The produced attention weights are taken out and will be forwarded to the attention-guided perturbation branch for integration.

**Decoder.** The decoder aims to decode the pretrained features of *normal* data in the training set. In our framework, we simply adopt a plain vision-transformer-based decoder thanks to an auxiliary attention-based perturbation branch. During training, the decoder is guided to decode the attention-guided perturbed representations derived from the feature extractor. Note that our decoder is lightweight and has only four layers, yet it demonstrates strong empirical performance.

**Attention Mask Generation.** The goal of the auxiliary branch is to perturb normal input for training under the guidance of attention masks. The details are described below. To calculate the attention mask, we leverage the attention maps from the feature extractor and the momentum distillation of the decoder, which is formulated as below:

$$A_{\text{final}} = \Phi_{\text{norm}}(A_{\text{prior}}) + \Phi_{\text{norm}}(A_{\text{learn}})$$

where

$$\left\{ \begin{array}{l} \Phi_{\text{norm}} := \text{max-min normalization function.} \\ A_{\text{prior}} = \Phi_{\text{aggr}}(\{A_l\}_{l=1}^L) \\ A_{\text{learn}} = \Phi_{\text{aggr}}(\{A_k\}_{k=1}^K) \end{array} \right. \quad (2)$$

As discussed earlier, the attention weights from the feature extractor directly reflect the importance of each localization in the feature maps [54]. Therefore, based on the

extracted subset of attention weights  $\{A_l\}_{l=1}^L$ , we compute the prior attention mask by  $A_{\text{prior}} = \Phi_{\text{aggr}}(\{A_l\}_{l=1}^L)$ , where  $\Phi_{\text{aggr}}$  denotes the aggregation operation over the attention maps. For simplicity, we only apply element-wise average pooling on the attention maps.

Second, the attention weights within the decoder are learned to aggregate important contextual cues for reconstruction. Hence, we further propose to utilize it for attention mask generation. However, these attention weights fluctuate rapidly with high variance, especially at the beginning of the training. For stabilization, we employ mean-distillation [29], which includes an exponential-moving-average (EMA) version of the decoder as the teacher.

$$\theta_{\text{md}} = \eta \cdot \theta_{\text{md}} + (1 - \eta) \cdot \theta_{\text{dec}} \quad (3)$$

where  $\theta_{\text{md}}$  and  $\theta_{\text{dec}}$  denote the parameters of the teacher and student (*i.e.*, the decoder) models, respectively.  $\eta$  controls the weight assigned to previous teacher parameters. The self-attention weights  $\{A_k\}_{k=1}^K$  from the teacher are taken to compute the learnable attention masks by  $A_{\text{learn}} = \Phi_{\text{aggr}}(\{A_k\}_{k=1}^K)$ . Lastly, we derive the final mask as  $A_{\text{final}} = \Phi_{\text{norm}}(A_{\text{prior}}) + \Phi_{\text{norm}}(A_{\text{learn}})$  which will be utilized to guide the following noise-adding process.

**Attention-Guided Noise.** For unsupervised anomaly detection, synthesized anomalies play a critical role in learning a compact and discriminative boundary to discern normal and abnormal samples. Numerous approaches have been proposed [3, 32] for synthesizing anomalies that closely resemble real ones. Concerning the impracticality of synthesizing all types of real anomalies, we argue that focusing on critical locations and perturbing them at the feature level could be a more efficient strategy. Besides, by perturbing those critical and informative locations, the models are forced to reason the relations across different localizations more comprehensively. To this end, we simply add Gaussian noise weighted by the attention mask in the normal feature space to synthesize the hard abnormal samples. Specifically, a noise tensor  $\mathcal{E} \in \mathbb{R}^{H_f \times W_f \times C_f}$  is first generated with each entry simply drawn from an **i.i.d** Gaussian distribution  $\mathcal{N}(\mu, \sigma)$ . Then we add the noise tensor to the normal features  $F_{\text{clean}}$  for perturbation based on attention mask  $A_{\text{final}}$  as follows:

$$F' = F_{\text{clean}} + \mathcal{E} \odot (\alpha(t) \cdot \Phi_{\text{norm}}(A_{\text{final}}) + \beta) \quad (4)$$

where  $\odot$  means the elementwise product,  $\alpha(t)$  and  $\beta$  control the intensity of adding noise to the features, which linearly increases with the training epochs.  $\beta$  is a hyperparameter.  $\Phi_{\text{norm}}$  denotes the max-min normalization function. The value of  $\alpha(t)$  can be calculated by

$$\alpha(t) = \gamma \cdot \left( \frac{t}{T}(p - m) + m \right), \quad (5)$$

where  $\gamma$  represents the basic noise factor,  $p$  denotes the maximum noise intensity,  $m$  represents the minimum noise intensity,  $T$  represents the maximum training epoch and  $t$  represents the current training epoch.

In addition to introducing noise at the feature level, we also incorporate noise at the image level, guided by the attention mask  $A_{\text{final}}$ , resulting in improved performance. To achieve this, we first upsample  $A_{\text{final}}$  to match the image dimensions, producing  $A_{\text{img}} \in \mathbb{R}^{H \times W}$ . Subsequently, we progressively increase the mask ratio for binarization. Gaussian noise is also applied within the masked regions. Gradually increasing the mask ratio increases the difficulty of denoising the decoder, which helps model training.

### 3.3. Loss Function

During training, for each normal image  $I_{\text{normal}} \in \mathcal{X}_{\text{train}}$ , we aim to reconstruct its normal features  $F_{\text{clean}}$  from the perturbed counterparts at both the image and feature levels. Our total loss is derived as

$$L_{\text{total}} = \frac{1}{2}(L_{\text{feat}} + L_{\text{img,feat}}) \quad (6)$$

where  $L_{\text{feat}}$  indicates reconstruction by perturbing features, and  $L_{\text{img,feat}}$  represents reconstruction by perturbing image and features at the same time, which are defined below:

$$\begin{cases} L_{\text{feat}} = \frac{1}{H_f \times W_f} \text{MSE}(F_{\text{feat}}, F_{\text{clean}}) \\ L_{\text{img,feat}} = \frac{1}{H_f \times W_f} \text{MSE}(F_{\text{img,feat}}, F_{\text{clean}}) \end{cases} \quad (7)$$

where  $F_{\text{clean}}$  indicates the features of the pretrained encoder output without noise-added,  $F_{\text{feat}}$  represents the reconstructed features by perturbing features, and  $F_{\text{img,feat}}$  means the reconstructed features by perturbing images and features at the same time.

### 3.4. Anomaly Map

During inference, we utilize reconstruction errors to calculate the anomaly map. Given an input image  $I \in \mathcal{X}_{test}$  from the test set, we first forward it to our framework to calculate pixel-level reconstruction errors in the feature map with  $L_2$  distance. Let  $F_q \in \mathbb{R}^{H_f \times W_f \times C_f}$  and  $\hat{F}_q \in \mathbb{R}^{H_f \times W_f \times C_f}$  denote the input and output of the reconstruction network, the pixel-level reconstruction error  $M \in \mathbb{R}^{H_f \times W_f}$  in the feature space at each pixel location  $(h, w)$  is calculated by

$$M_{h,w} = \|F_{h,w} - \hat{F}_{h,w}\|_2 \quad (8)$$

We further upsample  $M$  to be the same size as the input image with bilinear interpolation to produce the final anomaly map. For the image level anomaly score, we simply compute the maximum value of the average-pooled  $M$ .

## 4. Experiment

### 4.1. Experimental Setups

**Datasets.** *MVTec-AD* [1] is one of the most widely used industrial anomaly detection datasets. It has a training set consisting of 3629 normal images and a test set of 467/1,258 normal/anomaly images. All the images are divided into 15 categories. In this paper, we conduct experiments with two settings. One involves training a single model for all classes (multi-class setting), while the other involves training a separate model for each class (one-class setting). The former is a more efficient yet challenging task.

*VisA* [55] is another challenging anomaly detection dataset. It has a total of 10,821 images divided into 12 different categories. The training set has 8,659 normal images, and the test set includes 962/1,200 normal/anomaly images, providing a comprehensive benchmark for evaluating detection performance.

*MVTec-3D* [56] is a collection of 4,147 scans obtained through the industrial 3D sensor. It covers 10 different categories, each accompanied by both RGB images and corresponding 3D point cloud data. The training set consists of 2,656 images that include only anomaly-free samples. The test set comprises 1,197 images, which encompass both normal and anomalous

samples. In our experiments conducted, only use the RGB images, with the 3D point cloud data not being considered.

**Evaluation Metrics.** Referring to prior research [26, 3, 2], we report the anomaly detection and localization performance with Image-level and Pixel-level Area Under the Receiver Operating Curve, denoted by I-AUC and P-AUC respectively. We also adopt Per-Region-Overlap[57] to better evaluate model’s capability, denoted by PRO.

**Implement Details.** Each image is resized to  $224 \times 224$ . The feature extractor is initialized by pre trained DINO (ViT-S-16) [53], which is kept frozen during training. We employ AdamW [58] optimizer with a weight decay of  $1 \times 10^{-4}$ . We train our framework for 500 epochs on a single GPU (NVIDIA RTX 4090) with a batch size of 32. The learning rate is initially set to  $1 \times 10^{-3}$  and reduced by a factor of 0.1 after 200 epochs. The ratio of added noise at the image level linearly increases from 0.6 to 1.0 from the 100<sup>th</sup> to 400<sup>th</sup> epochs. The intensity of added noise  $\alpha$  at the feature level linearly increases from 0 to 1.0 from the 1<sup>st</sup> to 400<sup>th</sup> epochs. The hyper-parameter  $\eta$  in EMA is set to 0.9999, and the mean teacher is updated every 10 steps. Finally, for experiments under the few-shot setting, we perform a 32-fold data augmentation.

Table 1: Comparison of results on MVTec AD, VisA, and MVTec-3D (left: multi-class, right: one-class). \*: official code results. **Bold/underline**: best/second best.

Method	Multi-class Setting									One-class Setting			
	MVTec AD			VisA			MVTec-3D			Method	MVTec AD		
	I-AUC	P-AUC	PRO	I-AUC	P-AUC	PRO	I-AUC	P-AUC	PRO		I-AUC	P-AUC	PRO
DR $\bar{E}$ M*[3]	88.1	87.2	71.1	79.1	91.3	59.1	65.2	93.2	55.0	DR $\bar{E}$ M[3]	98.0	97.3	-
SimpleNet*[12]	85.1	88.9	86.5	87.2	96.8	81.4	-	-	-	RD4AD [7]	98.5	97.8	<b>93.9</b>
UniAD [26]	96.5	96.8	90.2	85.5	95.9	75.6	78.9	<u>96.5</u>	88.1	PatchCore[35]	99.1	<u>98.1</u>	<u>93.5</u>
DiAD[22]	97.2	96.8	90.7	86.8	96.0	75.2	<u>84.6</u>	96.4	87.8	DeSTSeg[6]	98.6	97.9	-
MSTAD[59]	<u>98.6</u>	97.2	-	-	-	-	-	-	-	SimpleNet[12]	<b>99.6</b>	<u>98.1</u>	-
MoEAD[47]	97.7	97.0	-	<b>93.1</b>	<b>98.7</b>	-	-	-	-	MSTAD[59]	98.3	97.5	-
ViTAD[60]	98.3	<u>97.7</u>	<u>91.4</u>	90.5	98.2	<u>85.1</u>	78.7	<b>98.0</b>	<u>91.3</u>	GLAD[61]	<u>99.3</u>	<b>98.6</b>	-
<b>Ours</b>	<b>98.7</b>	<b>98.0</b>	<b>92.9</b>	<u>92.3</u>	<u>98.4</u>	<b>85.5</b>	<b>84.9</b>	<b>98.0</b>	<b>92.9</b>	<b>Ours</b>	99.2	<u>98.3</u>	93.1

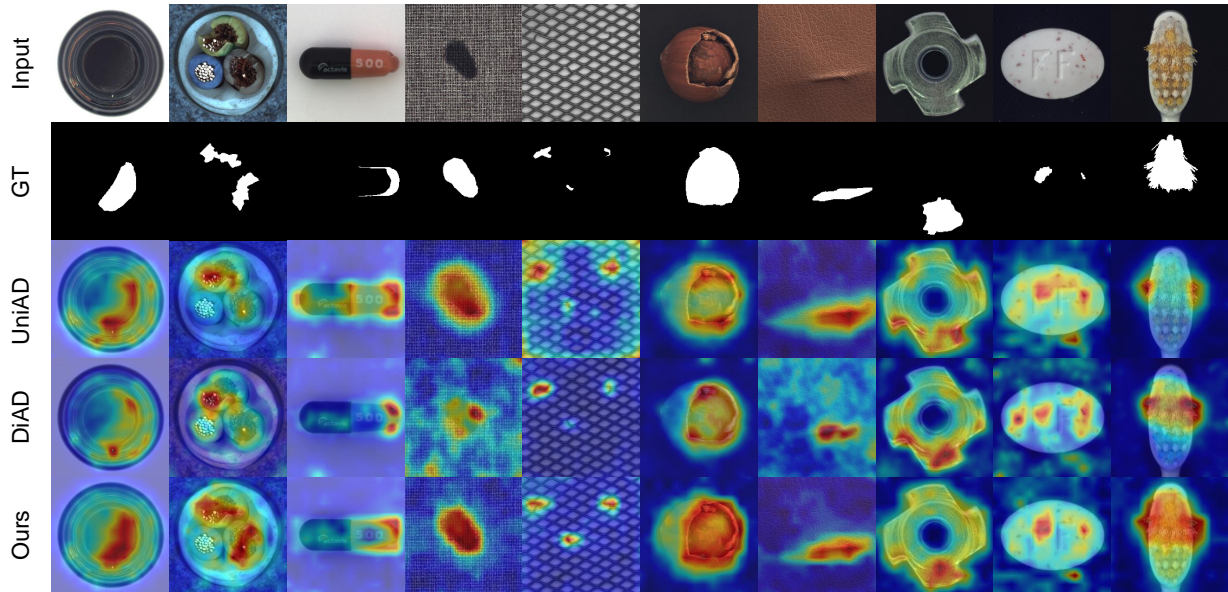


Figure 3: Qualitative illustration on MVTec-AD dataset.

#### 4.2. Anomaly Detection on MVTec-AD

**Baseline.** We comprehensively evaluated representative methods in both one-class and multi-class settings on MVTec-AD dataset. In the *multi-class setting*, we first compare our method with two representative one-class approaches: DRAEM[3] and SimpleNet[12], and then compare with methods specifically designed for the multi-class setting, including UniAD[26], RD4AD[7], DiAD[22], ViTAD[60], MoEAD[47] and MSTAD[59]. Note that all methods are trained under the multi-class scenario. In the *one-class setting*, the compared models includes: RD4AD[7], PatchCore[35], DRAEM[3], DeSTSeg[6], Simplenet[12], GLAD[61] and MSTAD[59].

**Evaluation on MVTec-AD under the multi-class setting.** As shown in Table 1, we conducted comprehensive comparative experiments on the MVTec-AD to demonstrate the superiority of our method. It can be observed that applying one-class methods to the multi-class scenario reflects undesirable performance. Furthermore, compared with existing multi-class methods, we outperform all of them, achieving the best 98.7% and 98.0% I-AUC and P-AUC, respectively. Our method outperforms the competitive ViTAD in both I-AUC(+0.4%) and P-AUC(+0.3%). In the more challenging PRO metric, our model also

achieves a great performance of 92.9%, with a 1.5% improvement over ViTAD. For comprehensive comparisons on each category, we note our method has the following compelling advantages:

- **Texture Categories:** As shown in Table 2, existing methods already achieve near-saturation performance on texture categories. For instance, in the multi-class setting, our method attains 100.0/99.2/95.6 on Carpet and 99.9/98.9/96.3 on Grid, with only marginal improvements over ViTAD (99.5/99.0/94.7 for Carpet).
- **Object Categories:** Significant improvements are observed on object categories, particularly those with small or fine-grained anomalies (e.g., Screw: +5.6% PRO over ViTAD; Transistor: +7.5% PRO). As evidenced by Screw’s P-AUC/PRO (99.0%/95.5%), our method better preserves defect details compared to ViTAD (99.0%/93.5%).

Table 2: Anomaly detection results on MVTEC AD under *multi-class setting*. \* denotes the reproduced results using the official code. **Bold** and underline indicate the best and the second best, respectively.

Category	DREM* [3]	SimpleNet* [12]	UniAD [26]	DiAD [14]	ViTAD [60]	<b>Ours</b>
	(ICCV 2021)	(CVPR 2023)	(NeurIPS 2022)	(AAAI 2024)	(CUIV 2025)	
I-AUC / P-AUC / PRO (%)						
Bottle	97.5 / 87.6 / 80.7	97.7 / 91.2 / 90.6	<u>99.7</u> / 98.1 / 93.2	<u>99.7</u> / 98.4 / -	<b>100.0</b> / <u>98.8</u> / <u>94.3</u>	<b>100.0</b> / <b>99.1</b> / <b>95.0</b>
Cable	57.8 / 71.3 / 40.1	87.6 / 88.1 / 85.4	95.2 / <u>97.3</u> / 85.7	94.8 / 96.8 / -	<u>98.5</u> / 96.2 / <u>90.2</u>	<b>99.7</b> / <b>98.0</b> / <b>92.9</b>
Capsule	65.3 / 50.5 / 27.3	78.3 / 89.7 / 84.5	86.9 / <b>98.5</b> / 89.7	89.0 / 97.1 / -	<b>95.4</b> / <u>98.3</u> / <u>92.0</u>	<u>93.8</u> / <b>98.5</b> / 91.9
Hazelnut	93.7 / 96.9 / 78.7	99.2 / 95.7 / 87.4	<u>99.8</u> / 98.1 / 92.9	99.5 / 98.3 / -	<u>99.8</u> / <b>99.0</b> / <b>95.2</b>	<b>100.0</b> / <u>98.9</u> / <u>93.6</u>
Metal_nut	72.8 / 62.2 / 66.4	85.1 / 90.9 / 85.2	99.2 / 94.8 / 84.7	99.1 / <b>97.3</b> / -	<u>99.7</u> / <u>96.4</u> / <u>92.4</u>	<b>100.0</b> / 95.9 / <b>92.6</b>
Pill	82.2 / 94.4 / 53.9	78.3 / 89.7 / 81.9	93.7 / 95.0 / 94.7	95.7 / 95.7 / -	<u>96.2</u> / <b>98.7</b> / <u>95.3</u>	<b>97.6</b> / <u>98.2</u> / <b>96.2</b>
Screw	<b>92.0</b> / 95.5 / 55.2	45.5 / 93.7 / 84.0	87.5 / <u>98.3</u> / <u>94.9</u>	90.7 / 97.9 / -	91.3 / <b>99.0</b> / 93.5	<u>91.8</u> / <b>99.0</b> / <b>95.5</b>
Toothbrush	90.6 / 97.7 / 68.9	94.7 / 97.5 / 87.4	94.2 / 98.4 / 88.0	<u>99.7</u> / <u>99.0</u> / -	98.9 / <b>99.1</b> / <u>90.9</u>	<b>100.0</b> / 98.9 / <b>91.2</b>
Transistor	74.8 / 64.5 / 39.0	82.0 / 86.0 / 83.2	<b>99.8</b> / <b>97.9</b> / <b>93.3</b>	<b>99.8</b> / <u>95.1</u> / -	<u>98.8</u> / 93.9 / 76.8	98.7 / 93.8 / <u>84.3</u>
Zipper	98.8 / <b>98.3</b> / <b>91.9</b>	<u>99.1</u> / 97.0 / 90.7	95.8 / 96.8 / <u>91.6</u>	95.1 / 96.2 / -	97.6 / 95.9 / 87.2	<b>99.7</b> / <u>97.6</u> / 90.5
Carpet	98.0 / 98.6 / 93.1	95.9 / 92.4 / 90.6	<u>99.8</u> / 98.5 / 93.6	99.4 / 98.6 / -	99.5 / <u>99.0</u> / <u>94.7</u>	<b>100.0</b> / <b>99.2</b> / <b>95.6</b>
Grid	99.3 / <u>98.7</u> / 92.1	49.8 / 46.7 / 88.6	98.2 / 96.5 / 91.1	98.5 / 96.6 / -	<u>99.7</u> / 98.6 / <u>95.8</u>	<b>99.9</b> / <b>98.9</b> / <b>96.3</b>
Leather	98.7 / 97.3 / 88.5	93.9 / 96.9 / 92.7	<b>100.0</b> / <u>98.8</u> / 96.5	<u>99.8</u> / <u>98.8</u> / -	<b>100.0</b> / <b>99.6</b> / <b>97.9</b>	<b>100.0</b> / 97.5 / <u>97.6</u>
Tile	<u>99.8</u> / <b>98.0</b> / <b>97.0</b>	93.7 / 93.1 / 90.6	99.3 / 91.8 / 78.6	96.8 / 92.4 / -	<b>100.0</b> / 96.6 / 87.0	<b>100.0</b> / <u>97.4</u> / <u>90.2</u>
Wood	<b>99.8</b> / 96.0 / <b>94.2</b>	95.2 / 84.8 / 76.3	98.6 / 93.2 / 85.0	<u>99.7</u> / 93.3 / -	98.7 / <u>96.4</u> / 88.0	98.9 / <b>96.6</b> / <u>90.2</u>
Mean	88.1 / 87.2 / 71.1	85.1 / 88.9 / 86.5	96.5 / 96.8 / 90.2	97.2 / 96.8 / 90.7	<u>98.3</u> / <u>97.7</u> / <u>91.4</u>	<b>98.7</b> / <b>98.0</b> / <b>92.9</b>

The qualitative comparison in Figure 3 demonstrates the superior anomaly localization capability of our method compared to DiAD and UniAD. As shown in columns 4 and 10, our

approach achieves exceptional precision in handling geometrically complex objects (toothbrushes) and textured surfaces (carpets). The heatmaps which generate by our model accurately align with anomaly contours at the pixel level. For more qualitative result, Figure 4 illustrates our method’s localization performance on the MVTec-AD dataset, where the first six columns represent object categories and the last three columns show texture categories. Our model demonstrates excellent performance on both types of anomalies. For challenging micro-cracks (7th row, 7th column), the predicted heatmap (7th row, 9th column) achieves precise anomaly localization, particularly in capturing subtle structural defects. When dealing with damages that are difficult to distinguish from background patterns (10th row, 7th column), our model’s heatmap achieves pixel-level registration with ground truth masks. For more challenging object cases, the attention-guided perturbation network not only accurately localizes object deformations (6th row, 1st column) but also effectively identifies fine cracks in foreground objects (1st row, 4th column).

The comprehensive qualitative results further reveal that our model maintains robust performance on different categories. These visual results, combined with detailed case studies, fully demonstrate the competitive performance of our proposed framework across all MVTec-AD categories, complementing and reinforcing our quantitative evaluation.

**Evaluation on MVTec-AD under the one-class setting.** As shown in Table 1, we can observe that compared with the two synthetic data-based methods, DRAEM [3] and DeSTSeg [35], we outperform them by a large margin. Specifically, compared with DRAEM, we outperform it by 1.2% and 1.0% in I-AUC and P-AUC, respectively. And compared to DeSTSeg, we also bring gains of 0.6% I-AUC and 0.4% P-AUC. Moreover, we achieved the best localization result of 98.3% P-AUC, while the detection performance is slightly lower than SimpleNet, ranking second among previous arts. It should be noted that when SimpleNet is adapted to the multi-class setup, its performance significantly drops, as evidenced in Table 1. In contrast, our method demonstrates robust performance across both setups, highlighting its strong generalization capability and suitability for real-world applications. Similarly, compared to the existing GLAD [61], which possesses the best localization performance, the proposed method remains competitive, achieving a P-AUC score just 0.3%

lower.

Table 3: Comparison of image-level/pixel-level results on MVTEC AD under *one-class setting*. \* denotes the reproduced results using the official code. **Bold** and underline indicate the best and the second best, respectively.

Category	DRÆM [3] (ICCV 2021)	RD4AD [62] (CVPR 2022)	PatchCore [11] (CVPR 2022)	DeSTSeg [6] (CVPR 2023)	SimpleNet [12] (CVPR 2023)	GLAD [61] (ECCV 2024)	Ours
	I-AUC / P-AUC / PRO (%)						
Bottle	99.2 / <u>99.1</u> / -	<b>100.0</b> / 98.7 / 96.6	<b>100.0</b> / 98.6 / -	- / <b>99.2</b> / -	<b>100.0</b> / 98.0 / -	<b>100.0</b> / 98.9 / -	<b>100.0</b> / <u>99.1</u> / 94.6
Cable	<u>99.9</u> / 97.6 / -	95.0 / 97.4 / 91.0	99.5 / <u>98.4</u> / -	- / 97.3 / -	94.8 / 96.8 / -	<u>99.9</u> / 98.1 / -	<b>100.0</b> / <b>98.7</b> / 93.9
Capsule	<u>98.5</u> / 94.3 / -	96.3 / 98.7 / 95.8	98.1 / 98.8 / -	- / <b>99.1</b> / -	97.7 / <u>98.9</u> / -	<b>99.5</b> / 98.5 / -	97.9 / 98.3 / 90.4
Hazelnut	<b>100.0</b> / <b>99.7</b> / -	99.9 / 98.9 / 95.5	<b>100.0</b> / 98.7 / -	- / <u>99.6</u> / -	<b>100.0</b> / 97.9 / -	<b>100.0</b> / 99.5 / -	<b>100.0</b> / 99.0 / 94.4
MetalNut	98.7 / <b>99.5</b> / -	<b>100.0</b> / 97.3 / 92.3	<b>100.0</b> / 98.4 / -	- / 98.6 / -	<b>100.0</b> / <u>98.8</u> / -	<b>100.0</b> / <u>98.8</u> / -	<b>100.0</b> / 97.0 / 91.5
Pill	<u>98.9</u> / 97.6 / -	96.6 / 98.2 / 96.4	96.6 / 97.4 / -	- / <b>98.7</b> / -	<b>99.0</b> / <u>98.6</u> / -	98.1 / 97.9 / -	98.2 / <u>98.6</u> / 96.4
Screw	93.9 / 97.6 / -	97.0 / <b>99.6</b> / 98.2	<u>98.1</u> / <u>99.4</u> / -	- / 98.5 / -	<b>98.2</b> / 99.3 / -	96.9 / 99.1 / -	97.2 / 99.3 / 96.7
Toothbrush	<b>100.0</b> / 98.1 / -	99.5 / 99.1 / 94.5	<b>100.0</b> / 98.7 / -	- / <u>99.3</u> / -	99.7 / 98.5 / -	<b>100.0</b> / <b>99.4</b> / -	97.2 / 98.9 / 90.3
Transistor	93.1 / 90.9 / -	96.7 / 92.5 / 78.0	<b>100.0</b> / 96.3 / -	- / 89.1 / -	<b>100.0</b> / <b>97.6</b> / -	98.3 / 96.2 / -	99.5 / <u>97.3</u> / 91.3
Zipper	<b>100.0</b> / 98.8 / -	98.5 / 98.2 / 95.4	99.4 / 98.8 / -	- / <b>99.1</b> / -	<u>99.9</u> / <u>98.9</u> / -	98.5 / 97.9 / -	99.3 / 97.4 / 93.0
Carpet	97.0 / 95.5 / -	98.9 / 98.9 / 97.0	98.7 / <u>99.0</u> / -	- / 96.1 / -	<u>99.7</u> / 98.2 / -	99.0 / 98.5 / -	<b>100.0</b> / <b>99.2</b> / 95.5
Grid	<u>99.9</u> / <b>99.7</b> / -	<b>100.0</b> / 99.3 / 97.6	98.2 / 98.7 / -	- / <b>99.1</b> / -	<u>99.7</u> / 98.8 / -	<b>100.0</b> / <u>99.6</u> / -	<b>100.0</b> / 98.9 / 96.2
Leather	<b>100.0</b> / 98.6 / -	<b>100.0</b> / 99.4 / 99.1	<b>100.0</b> / 99.3 / -	- / <u>99.7</u> / -	<b>100.0</b> / 99.2 / -	<b>100.0</b> / <u>99.8</u> / -	<b>100.0</b> / 99.5 / 97.7
Tile	99.6 / <b>99.2</b> / -	99.3 / 95.6 / 90.6	98.7 / 95.6 / -	- / 98.0 / -	<u>99.8</u> / 97.0 / -	<b>100.0</b> / <u>98.7</u> / -	<b>100.0</b> / 97.5 / 89.1
Wood	99.1 / 96.4 / -	99.2 / 95.3 / 90.9	99.2 / 95.0 / -	- / <u>97.7</u> / -	<b>100.0</b> / 94.5 / -	<u>99.4</u> / <b>98.4</b> / -	98.8 / 96.7 / 88.5
Mean	98.0 / 97.3 / -	98.5 / 97.8 / <b>93.9</b>	99.1 / 98.1 / <u>93.5</u>	98.6 / 97.9 / -	<b>99.6</b> / 98.1 / -	<u>99.3</u> / <b>98.6</b> / -	99.2 / <u>98.3</u> / 93.1

For more details on each category, As shown in Table 3, our method achieves a leading performance even when trained on single-class normal data. It should be noted that our performance under multi-class setting is comparable to our multi-class results. However, existing methods like SimpleNet can attain near-saturation levels (e.g., 99.6% mean I-AUC) but with much inferior performance on the multi-class setting (see Table 1). It is also worth mentioning that our approach has achieved 100% I-AUC on 7 categories (Bottle, Hazelnut, Metalnut, Carpet, Grid, Leather, Tile), surpassing or matching state-of-the-art results. Based on the results, we can draw the following two conclusions:

1) On challenging texture categories like Carpet and Grid, we attain a perfect 100% I-AUC with 99.2% and 98.9% P-AUC, respectively. This outperforms SimpleNet (99.7%/98.2% for Carpet) and PatchCore (98.7%/98.7% for Grid), demonstrating that our attention-guided perturbation strategy effectively preserves structural consistency while amplifying subtle anomalies.

2) For objects requiring fine-grained defect localization (e.g., Screw: 97.2% I-AUC/99.3% P-AUC/96.7% PRO), our method significantly improves PRO scores by 1.4–5.2% over RD4AD and PatchCore. This highlights the advantage of dual-domain attention in distinguishing micro-defects from real anomalies.

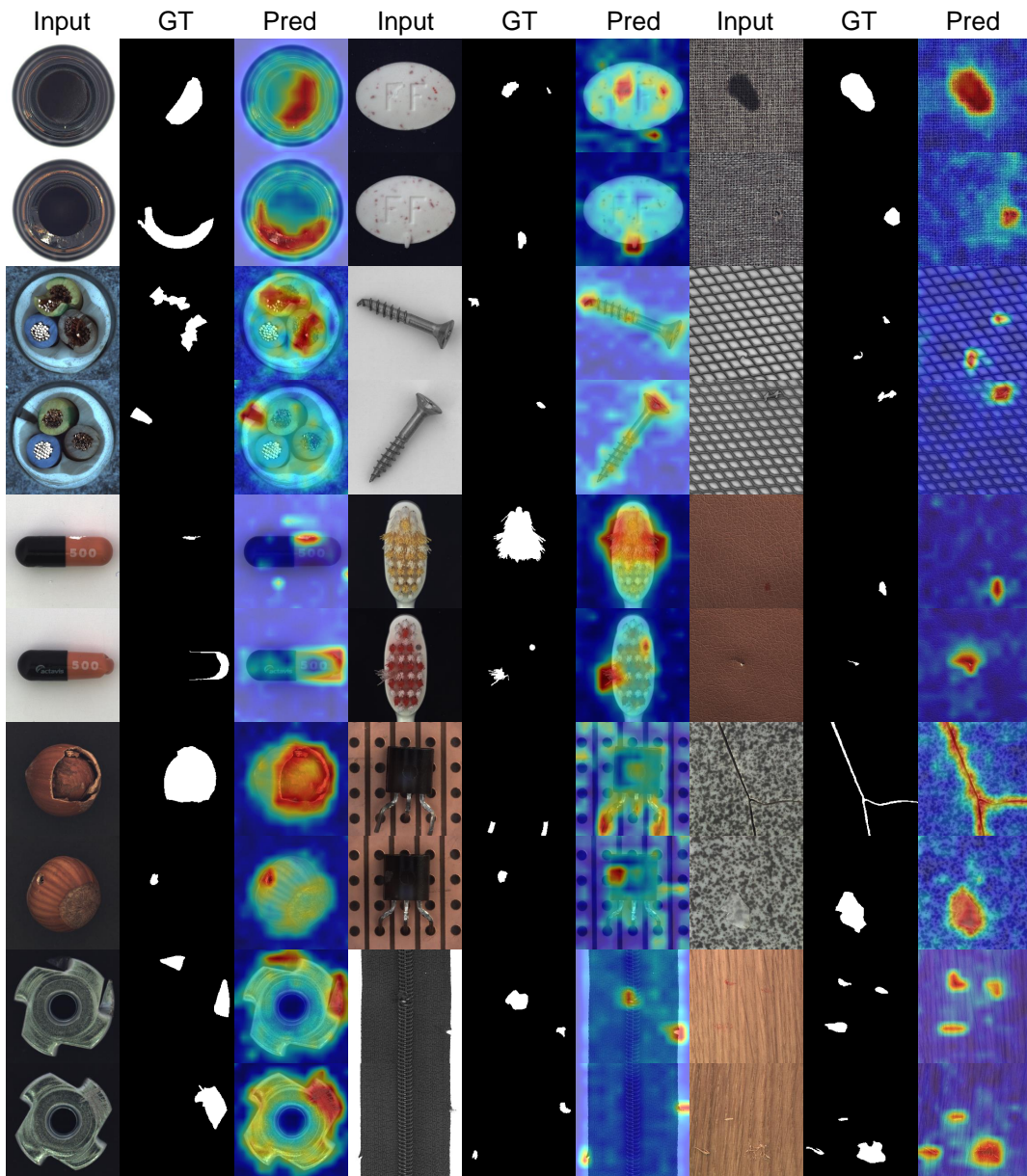
Overall, the detailed experience results for each category are further evidence of the powerful ability of our attention-guided perturbation network.

### 4.3. Anomaly Detection on VisA and MVTec-3D

**Baseline.** We further conduct experiments on the challenging VisA dataset under multi-class setting. For comprehensive comparisons, we have selected state-of-the-art models including DRAEM [3], UniAD [26], Simplenet [12], ViTAD [60] and DiAD [22]. On the MVTec-3D dataset, we compare our method with existing models, including DRAEM [3], UniAD [26], and DiAD [22].

**Evaluation on VisA.** As shown in Table 1, our method demonstrates competitive performance compared to existing approaches. Compared with the pioneering unified framework UniAD, we outperform it greatly by 6.8% and 3.5% in I-AUC and P-AUC, respectively. When compared with the pure ViT based model ViTAD, we outperform it in 10 out of 12 categories for detection and exceed it in 6 categories for localization. Specially, we improve upon it by 1.9%, 0.2% and 0.4% in I-AUC, P-AUC, and PRO, respectively. DiAD is one diffusion-based framework for multi-class anomaly detection. We surpass it by 1.5% and 1.2% in I-AUC and P-AUC, respectively. While our method exhibits marginally lower performance compared to the state-of-the-art MoEAD on VisA (e.g., 98.4% vs. 98.7% P-AUC), the experimental results across multiple datasets (e.g., MVTec AD 98.0% vs. 97.0% P-AUC) demonstrate its consistent effectiveness. Figure 5 illustrates our method’s localization performance on the Visa dataset. Rows 3 and 8 demonstrate precise detection of microscale anomalies, enabled by our multiscale feature integration that preserves fine-grained spatial details. The heatmap in Row 2, Column 3 highlights robust localization of significant structural anomalies, with activation maps tightly aligning to anomaly region boundaries.

**Evaluation on MVTec-3D.** As illustrated in Table 1, our approach outperforms all oth-



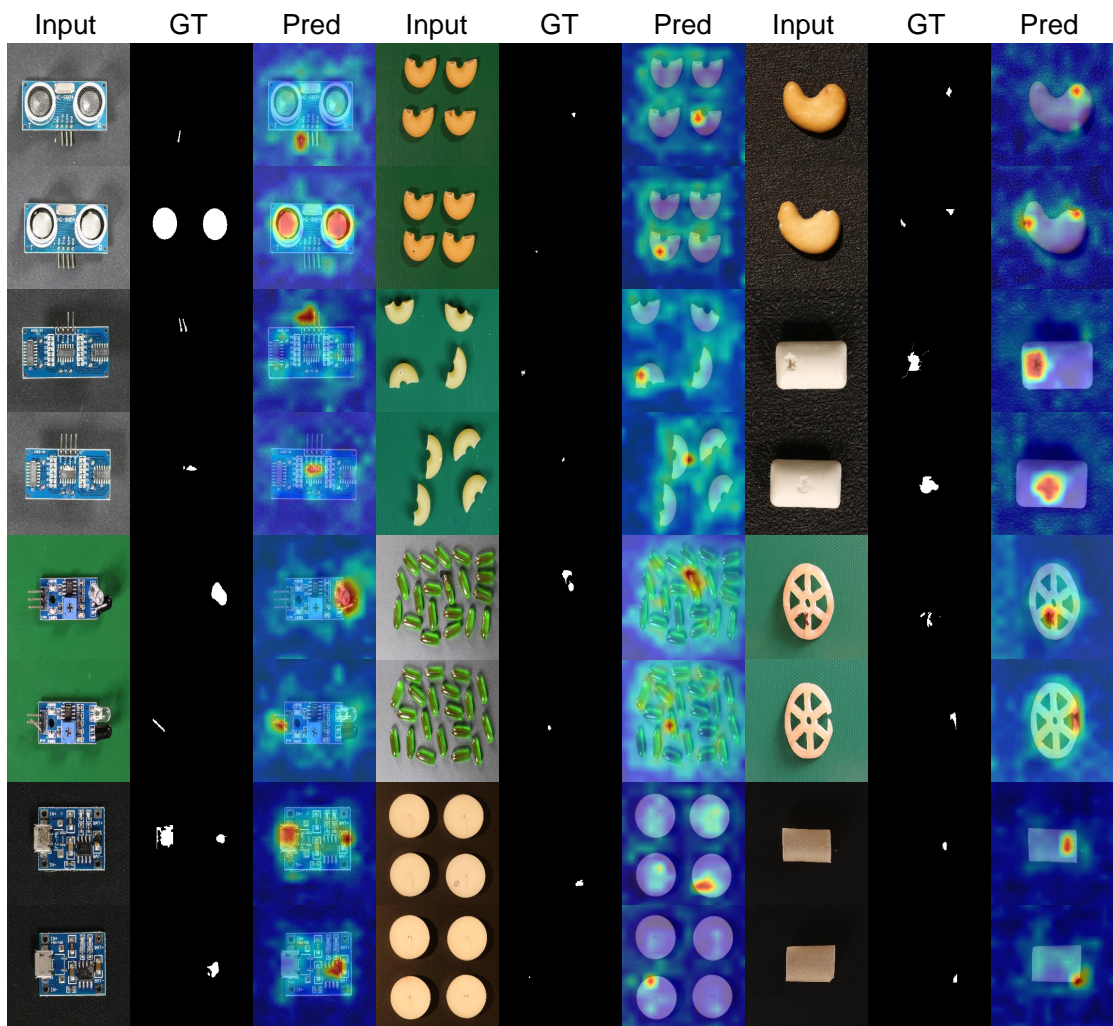


Figure 5: Qualitative illustration on Visa dataset.

ers across every metric evaluated. When compared to UniAD, our model demonstrates a considerable advantage, with improvements of 6.0%, 1.5%, and 4.8% in the I-AUC, P-AUC, and PRO, respectively. Compared to the diffusion-based method DiAD, our approach has achieved significant improvements in the evaluation metrics, with enhancements of 0.3%, 1.6%, and 5.1% in the I-AUC, P-AUC, and PRO, respectively. ViTAD, a competitive method based on Vision Transformers, also performs well. However, our method still outperforms ViTAD in I-AUC and PRO, further highlighting its effectiveness. These results substantiate the superior performance of our method.

Table 4: Ablation studies on attention-guided noise. ‘-’ means no noise is added. ‘R’ indicates adding random noise. ‘A’ denotes adding attention-guided noise.

Noise Type	No Noise	Only Random			Only Attention			Hybrid	
Image/Feature-level	-/-	R/-	-/R	R/R	A/-	-/A	A/A	A/R	R/A
I-AUC (%)	90.5	90.7	98.0	97.7	91.9	98.3	<b>98.7</b>	98.3	98.6
P-AUC (%)	95.5	95.5	97.7	97.8	96.0	97.7	<b>98.0</b>	97.8	97.8

#### 4.4. Ablation Study

In this subsection, we perform a thorough analysis of our framework on MVTec-AD under the multi-class setting.

**Attention-Guided Noise.** Table 4 studies the impact of noise addition techniques. We can observe that (1) without perturbing the input, this baseline model only achieves inadequate results of 90.5% and 95.5% detection (I-AUC) and localization (P-AUC) capacities, respectively. Such unsatisfactory results suggest that without perturbation the model also well-reconstruct the anomalous patterns. (2) When perturbing the input at the image level in a random manner, we observe a slight increase in I-AUC. However, adding noise at the feature level results in a significant increase, with gains of +7.5% I-AUC and +2.2% P-AUC, respectively. The phenomenon shows that random noise in the image and feature levels forces the model to learn normal patterns more comprehensively, effectively preventing the model from reconstructing anomaly regions. (3) When we introduce noise at the image-/feature-level using our Attention-guided method, compared to randomly adding noise at the same

levels, we achieve significant benefits. Specifically, in terms of I-AUC, we bring gains of 1.2% (91.9% *vs.* 90.7%) and 0.3% (98.3% *vs.* 98.0%), indicating the effectiveness of our strategy. Moreover, applying our strategy to both image and feature levels further enhances the model’s ability for anomaly detection and localization, achieving the best 98.7% I-AUC and 98.0% P-AUC. (4) Lastly, employing a hybrid noise addition approach only achieves suboptimal performance, further proving the superiority of our attention-guided strategy.

Table 5: Ablation studies on backbones and compare with the previous methods in multi-class setting.

Backbone	Method	I-AUC/P-AUC(%)
WideResNet-50	SimpleNet	85.1 / 88.9
	Ours	87.4 / 93.4
EfficientNet-b4	UniAD	96.5 / 96.8
	Ours	97.0 / 96.7
CLIP(ViT-B)	ViTAD-CLIP	71.2 / 81.6
	Ours	94.6 / 95.8
DINO(ViT-S)	ViTAD	98.3 / 97.7
	Ours	98.7 / 98.0

**Backbone.** To prove the generality of our method, we conduct comprehensive experiments using various backbones. As shown in 5, We employed two mainstream CNN-based backbones (Wide-Resnet-50[63] and EfficientNet-b4[64]) and two mainstream ViT-based backbones (CLIP[50] and DINO[53]) for our experiments. Compared to other mainstream anomaly detection frameworks, our method maintains competitive performance while using the same pre-trained backbones. Specifically, comparing to the ViTAD-CLIP, our method achieves a 23.4% improvement in I-AUC and a 14.2% improvement in P-AUC. When facing SimpleNet with WideResNet50, our method outperform with a 2.3% increase in I-AUC and a 4.5% increase in P-AUC. The results fully demonstrate the generality of the proposed attention-guided perturbation method.

**Multi-Layer Features.** 7 studies the impact of using multi-layer features. It can be observed that when utilizing deep features, the model demonstrates robust detection capacities, achieving 97.8% I-AUC. In contrast, employing shallow features exhibits desirable

localization abilities. Overall, integrating both shallow and deep features yields optimal performance.

Table 6: Ablation Studies on Noise Intensity  $\alpha$  at Feature-level and Attention Map. ‘D’ indicates just using the  $A_{\text{learn}}$  to guide the noise tensor, ‘L’ denotes just using the  $A_{\text{prior}}$  to guide the noise tensor, and ‘B’ means combining  $A_{\text{prior}}$  and  $A_{\text{learn}}$  to guide the noise tensor.

Components Options	Noise Intensity $\alpha$ at Feature-level				Attention map		
	0.5	1.0	1.5	0-1.0	L	D	B
I-AUC (%)	98.5	98.6	98.3	<b>98.7</b>	98.4	98.6	<b>98.7</b>
P-AUC (%)	97.9	97.9	97.9	<b>98.0</b>	97.9	97.9	<b>98.0</b>

**Mean Teacher Decoder.** Table 7 validates the effectiveness of the Mean Teacher decoder. Using the decoder of the reconstructed model to generate attention maps serves as the baseline. Introducing the Mean Teacher decoder results in an improvement of 0.3% for detection and 0.1% for localization. The experimental results demonstrate that the Mean Teacher decoder effectively mitigates the high variance of learnable attention weights during the initial training stages.

**Easy-to-Hard Noise Addition.** Recall that in Sec. 3.3, we use a hyperparameter  $\alpha$  to control the noise intensity at the feature level. 6 explores the impact of noise intensity. The experiments indicate that Easy-to-hard noise with suitable intensity helps the model to model the target distribution and achieve the best performance. Compared with fixed noise of different intensities, the I-AUC and P-AUC are slightly improved(0.1%-0.4%).

Table 7: Ablation Studies on Multi-level Features and Mean Distillation. ‘M.T.D’ indicates generating attention maps with mean distillation, while ‘w.o.’ means without mean distillation.

Components Options	Multi-layer				Mean Teacher	
	$f_{11}$	$f_2, f_5$	$f_8, f_{11}$	$f_2, f_5, f_8, f_{11}$	w.o.	M.T.D
I-AUC (%)	97.7	98.1	98.1	<b>98.7</b>	98.4	<b>98.7</b>
P-AUC (%)	97.8	97.0	97.8	<b>98.0</b>	97.9	<b>98.0</b>

**Attention Map.** Table 6 ablates two components for the final attention mask. We can observe that 1) using  $A_{\text{prior}}$  alone to guide the noise tensor already gives us satisfactory per-

formance, and 2) only  $A_{\text{learn}}$  guiding the noise tensor can achieve results close to optimal. 3) Finally, combining both obtains the highest performance. In particular, the strong performance achieved with learnable attention mask  $A_{\text{learn}}$  further demonstrates the superiority of attention-directed perturbation schemes. Specifically, the  $A_{\text{learn}}$  escalates denoising difficulty during normal distribution modeling, implementing efficient dynamic updating that prevents training plateauing in later phases. At the same time,  $A_{\text{prior}}$  provides good prior experience in the early stages of training. Their fusion optimally balances exploratory adaptation and exploitation of prior constraints.

Table 8: Efficiency comparison of different methods

Method	Learnable Parameters	FLOPs	FPS
DRÆM (ICCV 2021)	97.42M	198.15G	95.17
UniAD (NeurIPS 2022)	7.48M	<u>6.46G</u>	286.92
DeSTSeg (CVPR 2023)	32.37M	30.67G	<b>386.76</b>
SimpleNet (CVPR 2023)	<b>3.94M</b>	18.34G	63.66
DiAD (AAAI 2024)	1.33B	2.2T	-
<b>Ours</b>	<u>4.42M</u>	<b>5.63G</b>	<u>326.65</u>

#### 4.5. Efficiency Comparison with SoTAs

In addition to model performance, the efficiency of the model is a critical concern for practical applications. We evaluate the efficiency of various methods on a single RTX4090 GPU with a batch size of 32 using Learnable Parameters (M), Floating Point Operations (FLOPs), and Frames Per Second (FPS). As demonstrated in Table 8, our method ranks second in terms of both Learnable Parameters and FPS, while achieving the highest FLOPs. These results indicate that our proposed method effectively balances efficiency and performance, exhibiting strong potential for deployment on end-user devices.

#### 4.6. Extending to Few-shot Anomaly Detection

To further demonstrate the generality and potential of our framework, we conduct experiments on MVTec-AD under the challenging few-shot anomaly detection setups. We compared our method with some competitive methods and the models designed specifically

for few-shot setting, including SPADE [65], PaDiM [2], PatchCore [35], WinCLIP+ [49], RWDA [66], FastRcon [67], PromptAD [51]. As shown in Table 9, our method also obtains a leading few-shot anomaly detection performance, especially at pixel level. Specifically, our method achieves the best localization performance of 96.2% and 97.3% P-AUC under 2-shot and 4-shot settings. Compared to the competitive method PromptAD, which depends on a large pretrained CLIP model and intricate prompt tuning, we achieved a 0.8% P-AUC increase under 4-shot settings. Patchcore is a competitive anomaly detection model that relies on a resource-intensive memory bank to store nominal patch features. However, when faced with the more challenging few-shot setup, our approach remarkably outperforms it, with improvements of 6.4%, 7.0%, and 9.0% in I-AUC, and 3.0%, 2.9%, and 3.6% in P-AUC under the 4-shot, 2-shot, and 1-shot settings, respectively. The outstanding performance of our framework in few-shot settings highlights the unique advantages of our attention-guided perturbation strategy for scenarios with severely limited data.

Table 9: Comparison of image-level/pixel-level results on MVTec under *few shot setting*. **Bold** and underline indicate the best and the second best, respectively.

Method	1-shot	2-shot	4-shot
	I-AUC / P-AUC (%)		
SPADE (arXiv 2020)	81.0 / 91.2	82.9 / 92.0	84.8 / 92.7
PaDiM (ICPR 2020)	76.6 / 89.3	78.9 / 91.3	80.4 / 92.6
PatchCore (CVPR 2022)	83.4 / 92.0	86.3 / 93.3	88.8 / 94.3
WinCLIP+ (CVPR 2023)	93.1 / 95.2	<u>94.4</u> / 96.0	<u>95.2</u> / 96.2
RWDA (BMVC 2023)	<u>93.3</u> / -	94.0 / -	94.5 / -
FastRcon (ICCV 2023)	- / -	91.0 / 95.9	94.2 / <u>97.0</u>
PromptAD (CVPR 2024)	<b>94.6</b> / <b>95.9</b>	<b>95.7</b> / <b>96.2</b>	<b>96.6</b> / 96.5
<b>Ours</b>	92.4 / <u>95.6</u>	93.3 / <b>96.2</b>	<u>95.2</u> / <b>97.3</b>

## 5. Limitation

Similar to other unsupervised anomaly methods, the proposed method may be sensitive to noisy samples. In future investigations, it is worthy of focusing on framework robustness especially when abnormal samples corrupt the training set. Furthermore, our framework

mainly demonstrates the superior performance in industrial anomaly detection, while its generality in other areas such as medical anomaly detection and video anomaly analysis deserves more extensive investigation.

## 6. Conclusion

In this paper, we have proposed a simple yet effective reconstruction-based framework AGPNet to alleviate the issue of ‘identical shortcut’ for visual anomaly detection. It consists of a reconstruction branch for reconstruction and an auxiliary branch that aims to generate an attention mask for perturbations. To accommodate various samples across diverse categories, the attention mask is based on prior attention weights from the frozen feature extractor and mean-distillation of the decoder. The versatility of our framework is demonstrated on a variety of setups in visual anomaly detection, including multi-class-based, one-class-based, and few-shot ones, all with leading performance.

## 7. Acknowledge

This work is supported by the National Natural Science Foundation of China (No.62302188); Hubei Province Natural Science Foundation (No.2023AFB267); Fundamental Research Funds for the Central Universities (No.2662023XXQD001).

## References

- [1] P. Bergmann, M. Fauser, D. Sattlegger, C. Steger, Mvtec ad—a comprehensive real-world dataset for unsupervised anomaly detection, in: CVPR, 2019, pp. 9592–9600.
- [2] T. Defard, A. Setkov, A. Loesch, R. Audigier, Padim: a patch distribution modeling framework for anomaly detection and localization, in: ICPR, 2021, pp. 475–489.
- [3] V. Zavrtnik, M. Kristan, D. Skočaj, Draem—a discriminatively trained reconstruction embedding for surface anomaly detection, in: ICCV, 2021, pp. 8330–8339.
- [4] P. Bergmann, S. Löwe, M. Fauser, D. Sattlegger, C. Steger, Improving unsupervised defect segmentation by applying structural similarity to autoencoders, in: Proceedings of the 14th International Joint Conference on Computer Vision, Imaging and Computer Graphics Theory and Applications, 2019.

- [5] P. Bergmann, M. Fauser, D. Sattlegger, C. Steger, Uninformed students: Student-teacher anomaly detection with discriminative latent embeddings, in: *CVPR*, 2020, pp. 4183–4192.
- [6] X. Zhang, S. Li, X. Li, P. Huang, J. Shan, T. Chen, Destseg: Segmentation guided denoising student-teacher for anomaly detection, in: *CVPR*, 2023, pp. 3914–3923.
- [7] H. Deng, X. Li, Anomaly detection via reverse distillation from one-class embedding, in: *CVPR*, 2022, pp. 9737–9746.
- [8] H. M. Schlüter, J. Tan, B. Hou, B. Kainz, Natural synthetic anomalies for self-supervised anomaly detection and localization, in: *ECCV*, 2022, pp. 474–489.
- [9] Y. Cao, X. Xu, J. Zhang, Y. Cheng, X. Huang, G. Pang, W. Shen, A survey on visual anomaly detection: Challenge, approach, and prospect, *arXiv preprint arXiv:2401.16402* (2024).
- [10] J. Zhang, H. He, Z. Gan, Q. He, Y. Cai, Z. Xue, Y. Wang, C. Wang, L. Xie, Y. Liu, Ader: A comprehensive benchmark for multi-class visual anomaly detection, *arXiv preprint arXiv:2406.03262* (2024).
- [11] K. Roth, L. Pemula, J. Zepeda, B. Schölkopf, T. Brox, P. Gehler, Towards total recall in industrial anomaly detection, in: *CVPR*, 2022.
- [12] Z. Liu, Y. Zhou, Y. Xu, Z. Wang, Simplenet: A simple network for image anomaly detection and localization, in: *CVPR*, 2023, pp. 20402–20411.
- [13] Y. Liang, J. Zhang, S. Zhao, R. Wu, Y. Liu, S. Pan, Omni-frequency channel-selection representations for unsupervised anomaly detection, *TIP* (2023).
- [14] H. He, J. Zhang, H. Chen, X. Chen, Z. Li, X. Chen, Y. Wang, C. Wang, L. Xie, A diffusion-based framework for multi-class anomaly detection, in: *AAAI*, 2024.
- [15] Y. Cao, Q. Wan, W. Shen, L. Gao, Informative knowledge distillation for image anomaly segmentation, *Knowledge-Based Systems* 248 (2022) 108846.
- [16] H. He, Y. Bai, J. Zhang, Q. He, H. Chen, Z. Gan, C. Wang, X. Li, G. Tian, L. Xie, Mambaad: Exploring state space models for multi-class unsupervised anomaly detection, *arXiv preprint arXiv:2404.06564* (2024).
- [17] D. Gong, L. Liu, V. Le, B. Saha, M. R. Mansour, S. Venkatesh, A. v. d. Hengel, Memorizing normality to detect anomaly: Memory-augmented deep autoencoder for unsupervised anomaly detection, in: *ICCV*, 2019, pp. 1705–1714.
- [18] D. T. Nguyen, Z. Lou, M. Klar, T. Brox, Anomaly detection with multiple-hypotheses predictions, in: *ICML*, 2019, pp. 4800–4809.
- [19] M. Sabokrou, M. Khalooei, M. Fathy, E. Adeli, Adversarially learned one-class classifier for novelty detection, in: *CVPR*, 2018, pp. 3379–3388.
- [20] J. Kim, K. Jeong, H. Choi, K. Seo, Gan-based anomaly detection in imbalance problems, in: *Computer*

- Vision–ECCV 2020 Workshops: Glasgow, UK, August 23–28, 2020, Proceedings, Part VI 16, 2020, pp. 128–145.
- [21] X. Yan, H. Zhang, X. Xu, X. Hu, P.-A. Heng, Learning semantic context from normal samples for unsupervised anomaly detection, in: AAAI, volume 35, 2021, pp. 3110–3118.
  - [22] H. He, J. Zhang, H. Chen, X. Chen, Z. Li, X. Chen, Y. Wang, C. Wang, L. Xie, A diffusion-based framework for multi-class anomaly detection, in: Proceedings of the AAAI conference on artificial intelligence, volume 38, 2024, pp. 8472–8480.
  - [23] X. Zhang, N. Li, J. Li, T. Dai, Y. Jiang, S.-T. Xia, Unsupervised surface anomaly detection with diffusion probabilistic model, in: ICCV, 2023, pp. 6782–6791.
  - [24] Z. You, K. Yang, W. Luo, L. Cui, Y. Zheng, X. Le, Adtr: Anomaly detection transformer with feature reconstruction, in: International Conference on Neural Information Processing, 2022, pp. 298–310.
  - [25] Y. Shi, J. Yang, Z. Qi, Unsupervised anomaly segmentation via deep feature reconstruction, *Neurocomputing* 424 (2021) 9–22.
  - [26] Z. You, L. Cui, Y. Shen, K. Yang, X. Lu, Y. Zheng, X. Le, A unified model for multi-class anomaly detection, *NeurIPS* 35 (2022) 4571–4584.
  - [27] J. Deng, W. Dong, R. Socher, L.-J. Li, K. Li, L. Fei-Fei, Imagenet: A large-scale hierarchical image database, in: 2009 IEEE conference on computer vision and pattern recognition, 2009, pp. 248–255.
  - [28] A.-S. Collin, C. De Vleeschouwer, Improved anomaly detection by training an autoencoder with skip connections on images corrupted with stain-shaped noise, in: ICPR, 2021, pp. 7915–7922.
  - [29] A. Tarvainen, H. Valpola, Mean teachers are better role models: Weight-averaged consistency targets improve semi-supervised deep learning results, 2018. [arXiv:1703.01780](https://arxiv.org/abs/1703.01780).
  - [30] J. Liu, G. Xie, J. Wang, S. Li, C. Wang, F. Zheng, Y. Jin, Deep industrial image anomaly detection: A survey, *Machine Intelligence Research* 21 (2024) 104–135.
  - [31] J. Zipfel, F. Verworn, M. Fischer, U. Wieland, M. Kraus, P. Zschech, Anomaly detection for industrial quality assurance: A comparative evaluation of unsupervised deep learning models, *Computers & Industrial Engineering* 177 (2023) 109045.
  - [32] C.-L. Li, K. Sohn, J. Yoon, T. Pfister, Cutpaste: Self-supervised learning for anomaly detection and localization, in: CVPR, 2021, pp. 9664–9674.
  - [33] H. M. Schlüter, J. Tan, B. Hou, B. Kainz, Natural synthetic anomalies for self-supervised anomaly detection and localization, in: ECCV, 2022, pp. 474–489.
  - [34] V. Zavrtnik, M. Kristan, D. Skočaj, Dsr – a dual subspace re-projection network for surface anomaly detection, 2022. [arXiv:2208.01521](https://arxiv.org/abs/2208.01521).
  - [35] K. Roth, L. Pemula, J. Zepeda, B. Schölkopf, T. Brox, P. Gehler, Towards total recall in industrial anomaly detection, in: CVPR, 2022, pp. 14318–14328.

- [36] W. Liu, H. Chang, B. Ma, S. Shan, X. Chen, Diversity-measurable anomaly detection, in: CVPR, 2023, pp. 12147–12156.
- [37] J. Bae, J.-H. Lee, S. Kim, Pni: industrial anomaly detection using position and neighborhood information, in: ICCV, 2023, pp. 6373–6383.
- [38] V. Zavrtanik, M. Kristan, D. Skočaj, Reconstruction by inpainting for visual anomaly detection, PR 112 (2021) 107706.
- [39] H. M. Schlüter, J. Tan, B. Hou, B. Kainz, Natural synthetic anomalies for self-supervised anomaly detection and localization, in: European Conference on Computer Vision, 2022, pp. 474–489.
- [40] K. Zhou, Y. Xiao, J. Yang, J. Cheng, W. Liu, W. Luo, Z. Gu, J. Liu, S. Gao, Encoding structure-texture relation with p-net for anomaly detection in retinal images, in: ECCV, 2020, pp. 360–377.
- [41] Y. Xia, Y. Zhang, F. Liu, W. Shen, A. L. Yuille, Synthesize then compare: Detecting failures and anomalies for semantic segmentation, in: Computer Vision–ECCV 2020: 16th European Conference, Glasgow, UK, August 23–28, 2020, Proceedings, Part I 16, 2020, pp. 145–161.
- [42] F. Ye, C. Huang, J. Cao, M. Li, Y. Zhang, C. Lu, Attribute restoration framework for anomaly detection, IEEE TMM 24 (2020) 116–127.
- [43] T. Liu, B. Li, X. Du, B. Jiang, L. Geng, F. Wang, Z. Zhao, Fair: Frequency-aware image restoration for industrial visual anomaly detection, arXiv preprint arXiv:2309.07068 (2023).
- [44] Z. Li, N. Li, K. Jiang, Z. Ma, X. Wei, X. Hong, Y. Gong, Superpixel masking and inpainting for self-supervised anomaly detection., in: BMVC, 2020.
- [45] Y. Zhao, Omnia: A unified cnn framework for unsupervised anomaly localization, in: Proceedings of the IEEE/CVF Conference on Computer Vision and Pattern Recognition, 2023, pp. 3924–3933.
- [46] L. He, Z. Jiang, J. Peng, W. Zhu, L. Liu, Q. Du, X. Hu, M. Chi, Y. Wang, C. Wang, Learning unified reference representation for unsupervised multi-class anomaly detection, in: European Conference on Computer Vision, 2024, pp. 216–232.
- [47] S. Meng, W. Meng, Q. Zhou, S. Li, W. Hou, S. He, Moead: A parameter-efficient model for multi-class anomaly detection, in: European Conference on Computer Vision, Springer, 2024, pp. 345–361.
- [48] C. Huang, H. Guan, A. Jiang, Y. Zhang, M. Spratling, Y.-F. Wang, Registration based few-shot anomaly detection, in: European Conference on Computer Vision, Springer, 2022, pp. 303–319.
- [49] J. Jeong, Y. Zou, T. Kim, D. Zhang, A. Ravichandran, O. Dabeer, Winclip: Zero-/few-shot anomaly classification and segmentation, in: Proceedings of the IEEE/CVF Conference on Computer Vision and Pattern Recognition, 2023, pp. 19606–19616.
- [50] A. Radford, J. W. Kim, C. Hallacy, A. Ramesh, G. Goh, S. Agarwal, G. Sastry, A. Askell, P. Mishkin, J. Clark, et al., Learning transferable visual models from natural language supervision, in: International conference on machine learning, PMLR, 2021, pp. 8748–8763.

- [51] X. Li, Z. Zhang, X. Tan, C. Chen, Y. Qu, Y. Xie, L. Ma, Promptad: Learning prompts with only normal samples for few-shot anomaly detection, in: Proceedings of the IEEE/CVF Conference on Computer Vision and Pattern Recognition, 2024, pp. 16838–16848.
- [52] T. Reiss, N. Cohen, E. Horwitz, R. Abutbul, Y. Hoshen, Anomaly detection requires better representations, 2022. [arXiv:2210.10773](https://arxiv.org/abs/2210.10773).
- [53] M. Caron, H. Touvron, I. Misra, H. Jégou, J. Mairal, P. Bojanowski, A. Joulin, Emerging properties in self-supervised vision transformers, in: ICCV, 2021, pp. 9650–9660.
- [54] M. D. Zeiler, R. Fergus, Visualizing and understanding convolutional networks, in: Computer Vision—ECCV 2014: 13th European Conference, Zurich, Switzerland, September 6–12, 2014, Proceedings, Part I 13, 2014, pp. 818–833.
- [55] Y. Zou, J. Jeong, L. Pemula, D. Zhang, O. Dabeer, Spot-the-difference self-supervised pre-training for anomaly detection and segmentation, in: ECCV, 2022, pp. 392–408.
- [56] P. Bergmann, X. Jin, D. Sattlegger, C. Steger, The mvtec 3d-ad dataset for unsupervised 3d anomaly detection and localization, [arXiv preprint arXiv:2112.09045](https://arxiv.org/abs/2112.09045) (2021).
- [57] P. Bergmann, M. Fauser, D. Sattlegger, C. Steger, Uninformed students: Student-teacher anomaly detection with discriminative latent embeddings, in: 2020 IEEE/CVF Conference on Computer Vision and Pattern Recognition (CVPR), IEEE, 2020. URL: <http://dx.doi.org/10.1109/CVPR42600.2020.00424>. doi:10.1109/cvpr42600.2020.00424.
- [58] I. Loshchilov, F. Hutter, Decoupled weight decay regularization, 2019. URL: <https://arxiv.org/abs/1711.05101>. [arXiv:1711.05101](https://arxiv.org/abs/1711.05101).
- [59] B. Kang, Y. Zhong, Z. Sun, L. Deng, M. Wang, J. Zhang, Mstad: A masked subspace-like transformer for multi-class anomaly detection, Knowledge-Based Systems 283 (2024) 111186. URL: <https://www.sciencedirect.com/science/article/pii/S095070512300936X>. doi:<https://doi.org/10.1016/j.knosys.2023.111186>.
- [60] J. Zhang, X. Chen, Y. Wang, C. Wang, Y. Liu, X. Li, M.-H. Yang, D. Tao, Exploring plain vit features for multi-class unsupervised visual anomaly detection, Computer Vision and Image Understanding (2025) 104308.
- [61] H. Yao, M. Liu, Z. Yin, Z. Yan, X. Hong, W. Zuo, Glad: towards better reconstruction with global and local adaptive diffusion models for unsupervised anomaly detection, in: European Conference on Computer Vision, Springer, 2024, pp. 1–17.
- [62] H. Deng, X. Li, Anomaly detection via reverse distillation from one-class embedding, in: Proceedings of the IEEE/CVF conference on computer vision and pattern recognition, 2022, pp. 9737–9746.
- [63] K. He, X. Zhang, S. Ren, J. Sun, Deep residual learning for image recognition, 2015. URL: <https://arxiv.org/abs/1512.03385>. [arXiv:1512.03385](https://arxiv.org/abs/1512.03385).

- [64] M. Tan, Q. V. Le, Efficientnet: Rethinking model scaling for convolutional neural networks, 2020. URL: <https://arxiv.org/abs/1905.11946>. arXiv:1905.11946.
- [65] N. Cohen, Y. Hoshen, Sub-image anomaly detection with deep pyramid correspondences, arXiv preprint arXiv:2005.02357 (2020).
- [66] M. Tamura, Random word data augmentation with clip for zero-shot anomaly detection, arXiv preprint arXiv:2308.11119 (2023).
- [67] Z. Fang, X. Wang, H. Li, J. Liu, Q. Hu, J. Xiao, Fastrecon: Few-shot industrial anomaly detection via fast feature reconstruction, in: Proceedings of the IEEE/CVF International Conference on Computer Vision, 2023, pp. 17481–17490.